Modeling contamination migration on the *Chandra X-ray Observatory* — II

Stephen L. O'Dell[*a], Douglas A. Swartz[b], Neil W. Tice[c], Paul P. Plucinsky[d], Catherine E. Grant[c], Herman L. Marshall[c], Alexey A. Vikhlinin[d], and Allyn F. Tennant[a]

[a] NASA Marshall Space Flight Ctr., MSFC/ZP12, Huntsville, AL 35812, USA
[b] Universities Space Research Assoc., MSFC/ZP12, Huntsville, AL 35812, USA
[c] Massachusetts Institute of Technology, 77 Massachusetts Ave., Cambridge, MA 02139, USA
[d] Smithsonian Astrophysical Observatory, 60 Garden St., Cambridge, MA 02138, USA

ABSTRACT

During its first 14 years of operation, the cold (about -60°C) optical blocking filter of the Advanced CCD Imaging Spectrometer (ACIS), aboard the *Chandra X-ray Observatory*, has accumulated a growing layer of molecular contamination that attenuates low-energy x rays. Over the past few years, the accumulation rate, spatial distribution, and composition have changed. This evolution has motivated further analysis of contamination migration within and near the ACIS cavity. To this end, the current study employs a higher-fidelity geometric model of the ACIS cavity, detailed thermal modeling based upon temperature data, and a refined model of the molecular transport.

Keywords: X-ray astronomy, CCDs, contamination, modeling and simulation, spacecraft operations

1. INTRODUCTION

Noted for its arcsecond spectrometric imaging and high-resolution dispersive spectroscopy over the soft-x-ray band, the science system of the *Chandra X-ray Observatory*,[1, 2, 3, 4] (Figure 1) comprises the following x-ray components:

1. High-Resolution Mirror Assembly (HRMA), with 10-m focal length and 0.11 m^2 aperture area
2. Low-Energy Transmission Grating (LETG) and High-Energy Transmission Grating (HETG), insertable
3. High-Resolution Camera (HRC, microchannel plate) and Advanced CCD Imaging Spectrometer (ACIS)

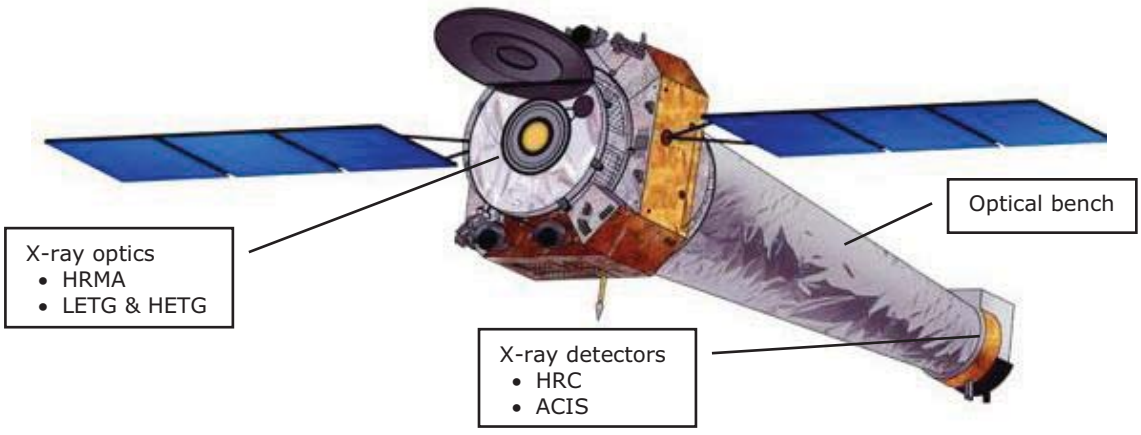

Figure 1. Illustration of the *Chandra X-ray Observatory*, showing the locations of the x-ray optics and the x-ray detectors, separated by the graphite-fiber-composite optical bench assembly.

[*] Contact author (SLO): stephen.l.odell@nasa.gov; voice +1 (256) 961-7776; fax +1 (256) 961-7522
Postal address: NASA/MSFC/ZP12; 320 Sparkman Drive NW; Huntsville, AL 35805-1912, USA

The Advanced CCD Imaging Spectrometer[5] (Figure 2) is *Chandra*'s most utilized science instrument. Its focal plane comprises a 2×2-CCD imaging array (ACIS-I), arranged for imaging over a 16.9′×16.9′ field, and a 1×6-CCD spectroscopy array (ACIS-S), arranged for reading dispersed spectra from *Chandra*'s objective transmission gratings. Each CCD has 1024×1024 24.0-μm-square pixels plus a shielded frame-store region. Two CCDs (both in the S array) are back-illuminated (BI) for more sensitive low-energy x-ray response; the remaining eight CCDs are front-illuminated (FI). To optimize CCD performance, ACIS employs passive radiative cooling compensated by electrical heaters to hold the CCD focal plane at about -120°C and the detector housing at about -60°C.

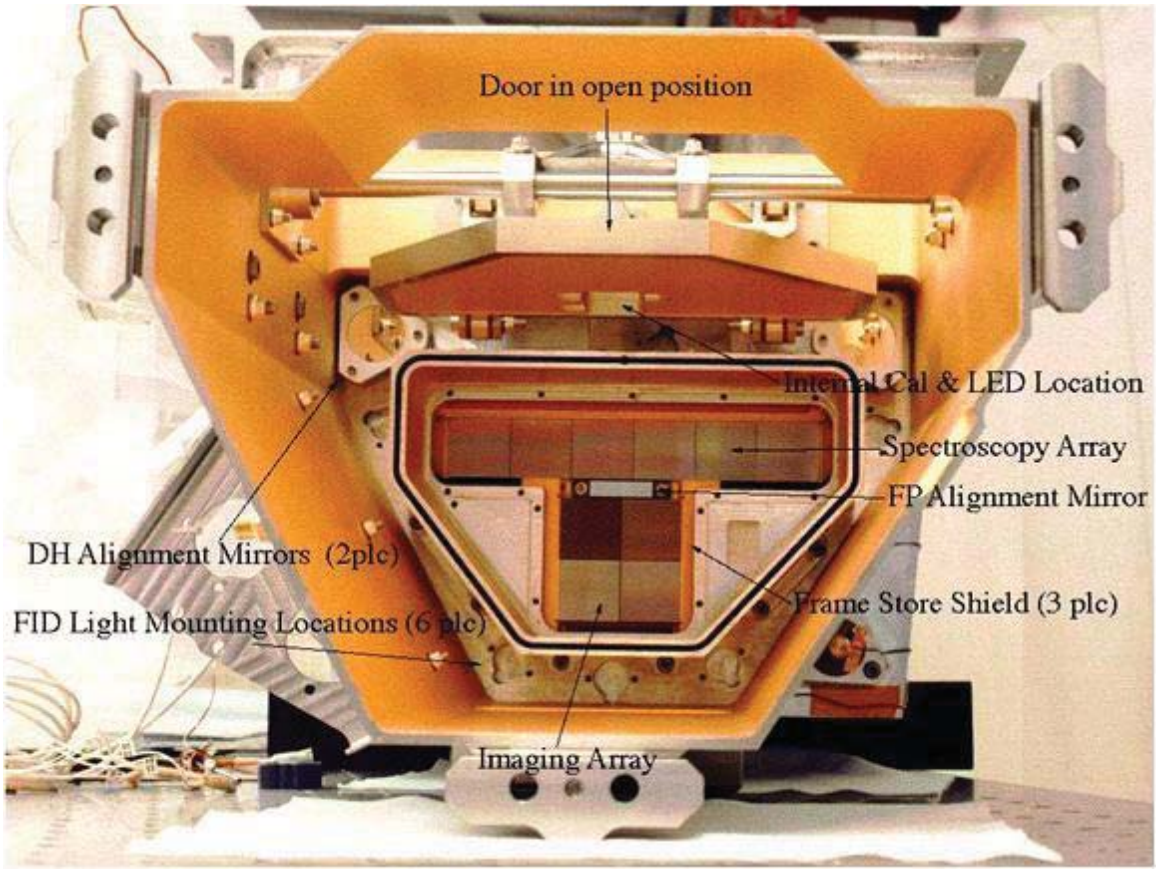

Figure 2. Top view of the engineering unit of *Chandra*'s Advanced CCD Imaging Spectrometer (ACIS), showing the 2×2-CCD ACIS-I and the 1×6-CCD ACIS-S focal planes. In the flight unit, aluminized-polyimide optical blocking filters OBF-I and OBF-S cover, respectively, the I and the S arrays. The OBFs reside within the "snoot" (with door sealed closed until *Chandra*'s on-orbit check-out), which in turn lies within the ACIS "collimator".

As CCDs are sensitive to visible-to-near-infrared light as well as to x radiation, ACIS-I and ACIS-S each utilize a double-side aluminized-polyimide optical blocking filter[6]—OBF-I and OBF-S, respectively—to suppress contamination by visible-band photons. Despite being quite thin—Al/Polyimide/Al = 120/200/40 nm (OBF-I), 100/200/30 nm (OBF-S)—the meshless Luxel™ filters are mechanically robust. A frame attached to the camera top holds OBF-I and OBF-S above the respective CCD array.

The outward face of the OBFs, the camera top, the inner and outer surfaces of the snoot, and the inner surface of the collimator bound the ACIS cavity (Figure 2), which connects to the large Telescope cavity. Near the end of the long optical bench opposite ACIS, the Telescope cavity vents to space through spacecraft vents and through the HRMA aperture (Figure 1). At about -60°C, the ACIS surfaces are by far the coldest surfaces within *Chandra*'s optical cavity. Based upon the observed attenuation of low-energy x rays[7] (§2), these cold surfaces have accumulated a layer (≈ 200 μg cm^{-2}) of an unidentified molecular contaminant over 14 years of operation. Although the accumulation of molecular contamination is 30 times pre-flight estimates, the total mass of contaminant is < 1 g.

After the 2002 finding that molecular contamination on the OBFs was accumulating faster than anticipated, the *Chandra* team performed a detailed study[8] of risks, benefits, and efficacy of baking ACIS. Although pre-flight contamination predictions indicated that an on-orbit bake would probably not be needed, the ACIS team retained a capability for on-orbit room-temperature bakes. Indeed, the ACIS team conducted numerous pre-flight bakes, plus one on-orbit bake early in the mission—in an (unsuccessful) effort to anneal radiation damage to the FI CCDs. Likewise, a thorough investigation by the *Chandra* team determined that room-temperature bakes present a credible risk neither to ACIS nor to the spacecraft. However, lacking definitive identification of the molecular contaminant(s)[9], contamination-migration simulations[10] indicated that the parameter space for a successful bake was small and that the bake might plausibly result in more contamination on the OBFs. Primarily for this reason, the *Chandra* team postponed indefinitely a decision on baking the ACIS.

During the decade since the bake-out study, the *Chandra* team continued to monitor the accumulation of molecular contamination on the ACIS OBFs through measurements of the increasing attenuation of low-energy x rays (§2). The observed evolution (§2.1) of the x-ray absorption depth indicates changes in rate, gradient, and composition of the contaminant(s) that are possibly correlated to a 2008 change in the temperature of the ACIS detector housing (§2.2). Recognizing that this possible correlation potentially provides additional constraints on the volatility of the molecular contaminant(s), we initiated a new contamination-migration study (§3). For this new investigation, we developed a more detailed geometric model (§3.1) of the ACIS cavity and utilize onboard temperature measurements to generate a higher-fidelity thermal model (§3.2), which we use for updated molecular-transport simulations (§3.3). Finally, we briefly summarize (§0) initial results of this new study, which is currently underway.

2. MOLECULAR CONTAMINATION ON ACIS FILTERS

As part of its continuing on-orbit calibration program, the *Chandra* team monitors the net efficiency of the ACIS CCDs, thus providing a measurement of the absorption depth of the molecular contamination on the OBFs. In this section, we provide an overview of the observed evolution of the contaminant (§2.1) and note a possible correlation of changes in the accumulated contamination with a change in the temperature of the ACIS camera body (§2.2) and, hence, of the edges of the OBFs. Such a correlation would be important, in that it potentially helps constrain the volatility of the accumulated contaminant(s).

2.1. Observed evolution

Various ACIS spectrometric and LETG/ACIS-S high-resolution spectroscopic observations measure x-ray absorption by contamination accumulated on the ACIS OBFs. Figure 3 displays ACIS-I and ACIS-S spectrometric measurements of the evolution over the mission, of the 0.7-keV absorption depth near the center of each OBF (left panel) and of the difference in absorption depth between outer and central regions of the OBF (right panel).

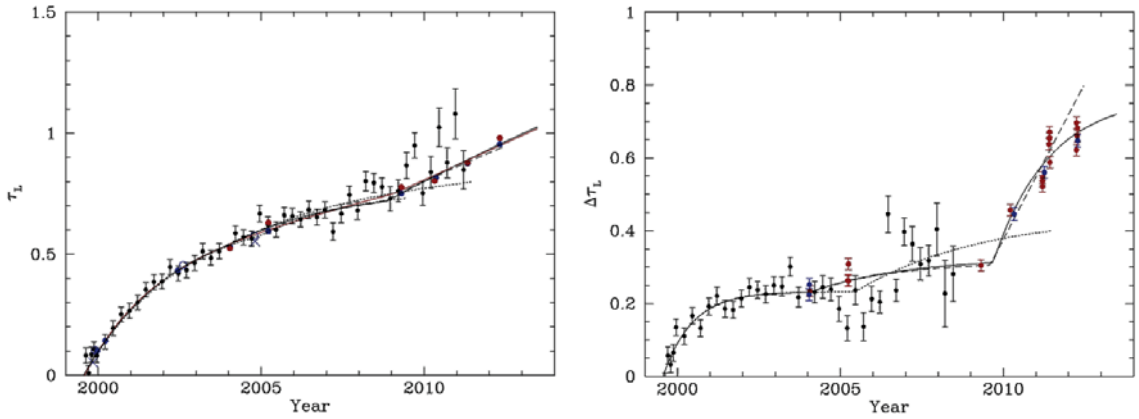

Figure 3. Evolution of the 0.7-keV absorption depth due to molecular contamination on the ACIS optical blocking filter (OBF). Left panel shows τ_L, the 0.7-keV absorption depth at the center of the OBF; right panel shows $\Delta\tau_L$, the 0.7-keV absorption depth near the OBF edge minus its value near the OBF center. Black symbols (with progressively larger error bars) denote Mn/Fe-L-complex measurements of the ACIS Fe^{55} external calibration source; red or blue symbols, measurements of the Abell 1795 cluster using ACIS-I or ACIS-S, respectively.

The plots in Figure 3 combine data obtained from measurements of the ACIS Fe^{55} external calibration source (obtained when ACIS is in the stowed position) and a series of pointed observations of the (extended) cluster of galaxies Abell 1795. As the Fe^{55} half-life is only 2.7 years, its utility for calibration has diminished substantially. Consequently, future spectrometric measurements of the absorption depth will rely primarily on observations of cosmic x-ray sources—such as A1795.

Figure 4 employs observations of A1795 to determine the gradient in the 0.7-keV absorption depth across the (BI) CCD S3, for four epochs. This plot shows that the gradient is quite flat over the middle half of the CCD rows but steepens toward the top or bottom of the CCD, near the OBF-S frame. As already evidenced in the right panel of Figure 3, the steepening of the gradient has become progressively more pronounced with time.

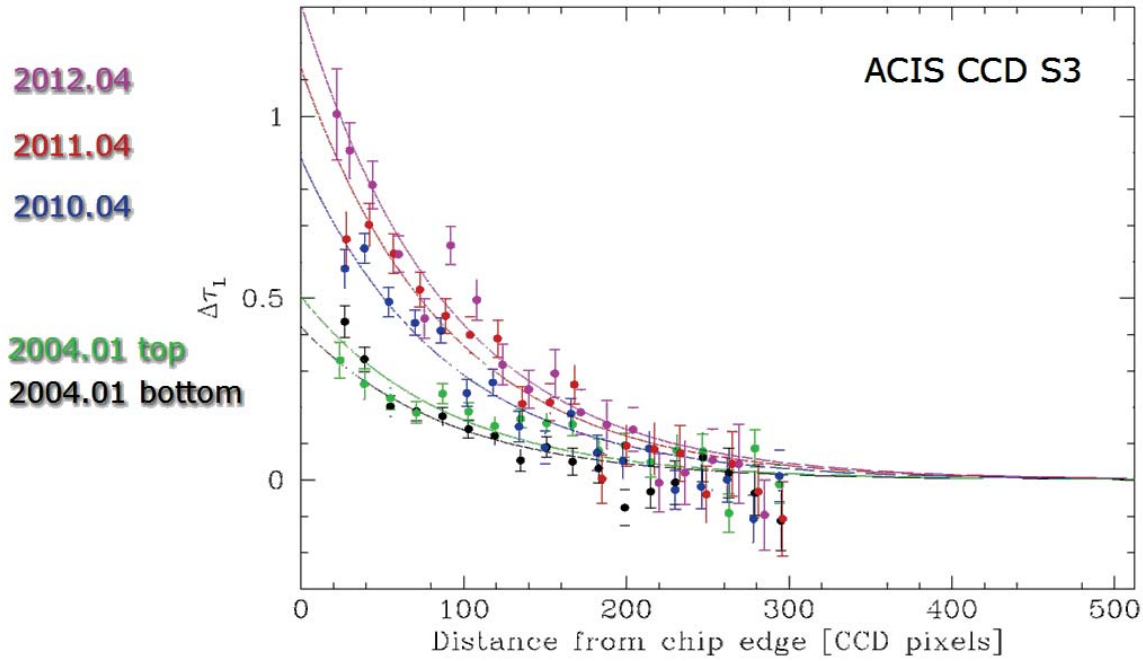

Figure 4. Gradient in the 0.7-keV absorption depth due to molecular contamination on the ACIS-S optical blocking filter (OBF-S), for 4 observational epochs. The plot shows $\Delta\tau_L$, absorption depth as a function of rows from the chip edge, minus absorption depth at the center rows for the back-illuminated S3 (centermost CCD of the S array). NB: ACIS CCDs have 1024 rows.

Returning to Figure 3, inspection of the left panel finds that the 0.7-keV absorption depth τ_L increased rapidly from the start of science operations in late 1999 but that the growth rate steadily subsided until about 2009, when the growth rate again increased. The right panel of Figure 3 shows that the edge-to-center gradient $\Delta\tau_L$ of the 0.7-keV absorption depth exhibits similar temporal behavior that is even more prominent.

Using LETG/ACIS-S high-resolution spectroscopy of cosmic x-ray sources, we find that the absorption depths of the atomic edges of the contaminant's constituent elements—carbon C, oxygen O, and fluorine F—also display a similar temporal behavior. Figure 5 displays the evolution of the mass column of C, O, and F on OBF-S, as determined by fitting the absorption edges of these elements to LETG/ACIS-S high-resolution spectroscopy of cosmic x-ray sources. The left panel shows the accumulation of these contaminant elements over the mission since the start of 2000 to mid 2013, for the nominal aim point (triangle and "x" symbols) and for calibration observations near the bottom edge of OBF-S (symbols enclosed by squares). The temporal behavior exhibited in the figure is similar—albeit not identical—to that in Figure 3, for the 0.7-keV absorption depth. The right panel of Figure 3 shows the accumulation *rate* of C and of O over the same time span. Although this plot is basically just the time derivative of the plot in the left panel, it perhaps illustrates more clearly the temporal evolution: The accumulation rate decreases from the beginning of science operations but then starts to increase around 2009. The right panel of Figure 5 also suggests a change in the composition of the accumulating molecular contamination: Most evident is the apparently very small rate of accumulation of oxygen-bearing contamination during 2004–2008.

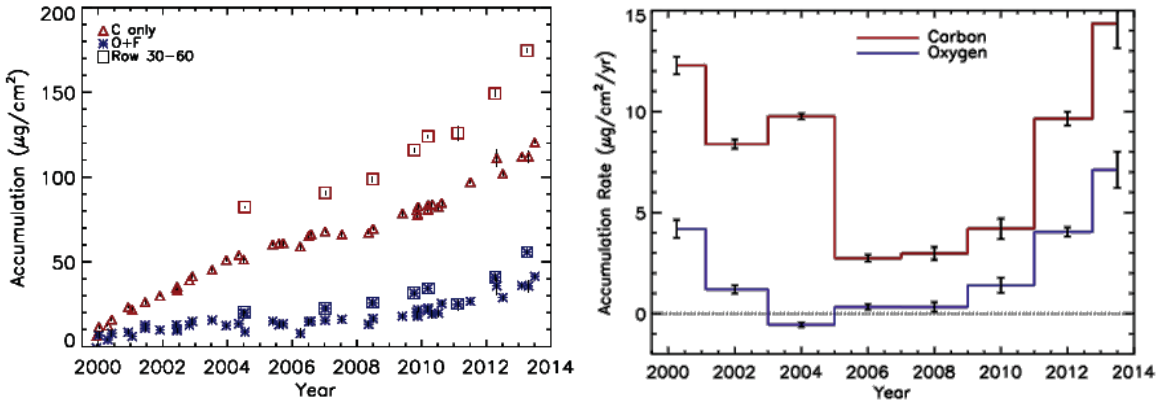

Figure 5. Evolution of the mass column of molecular contamination on the ACIS optical blocking filter (OBF), as determined from high-resolution spectra obtained using *Chandra*'s objective transmission gratings. Left panel shows the accumulated mass column of carbon (red triangles) and of oxygen and fluorine (blue "x") at the nominal spectroscopy aim point; square-enclosed symbols denote measurements close to the edge of OBF-S. Right panel displays the accumulation rate of carbon (upper red line) and of oxygen (lower blue line) near the center of OBF-S.

The salient features of the observed evolution (Figure 3 and Figure 5) of the molecular contaminant(s) on the ACIS OBFs are then these:

1. The accumulation rate decreased steadily from the start of science operations in late 1999.
2. The accumulation rate increased again around 2009.
3. Accumulation is significantly larger near the edges of the OBFs than near their centers.
4. The composition of the accumulated contamination also may have evolved.

2.2. Possible relation to temperature changes

Of the main features of the evolution of the molecular contamination (§2.1), the most curious was the increase in the accumulation rate that began about 2009. Recall that accumulation rate equals deposition rate minus vaporization rate. As contamination sources eventually deplete, an expected decline in the deposition rate naturally accounts for the early decrease in the accumulation rate onto the OBFs. The rise in the accumulation rate starting around 2009 would require either an increased deposition rate—e.g., a new source—or a decrease in the vaporization rate of contamination on the OBFs. The latter explanation—i.e., decreased vaporization rate—naturally occurs if the OBF temperatures were lowered. Indeed, the Chandra team in 2008 April turned OFF the ACIS detector-housing heater (Figure 6 left panel) in an effort to help maintain the ACIS focal-plane temperature near -120°C (right panel).

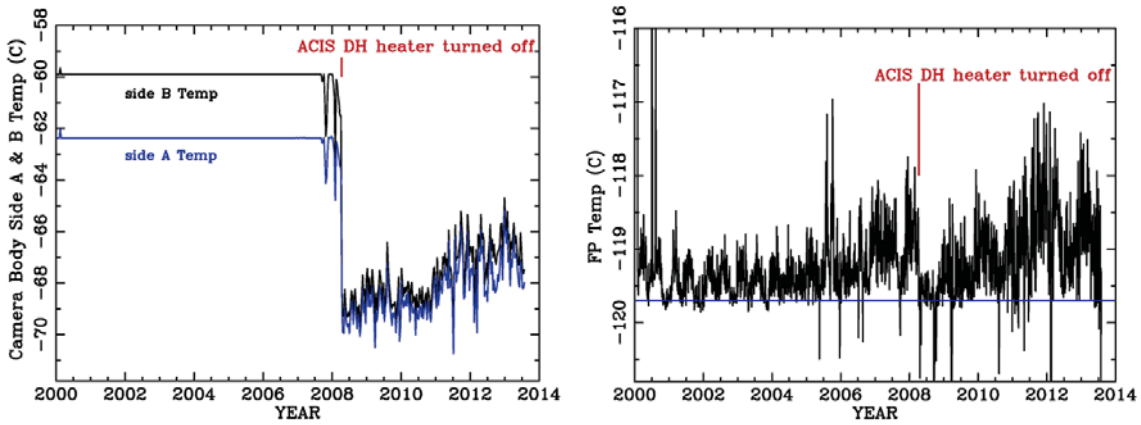

Figure 6. Recorded temperatures of the ACIS camera body (left panel) and of its CCD focal plane (right panel). Heaters held the camera body at a constant temperature until they were turned OFF in 2008 April, in order to help keep the focal-plane temperature near -120°C.

Turning OFF the ACIS detector-housing heater in 2008 April immediately lowered the temperature (Figure 6 left panel) of the ACIS camera top and OBF frames (and, hence, OBF edges) by about 8°C—approximately from -61°C to -69°C. As Figure 7 illustrates, an 8°C drop in temperature near -60°C dramatically lowers the vaporization rate—by a factor of 10–30. Thus, if the vaporization rate of a contaminant were initially comparable to the deposition rate, lowering the temperature would lower the vaporization rate and thus increase the accumulation rate.

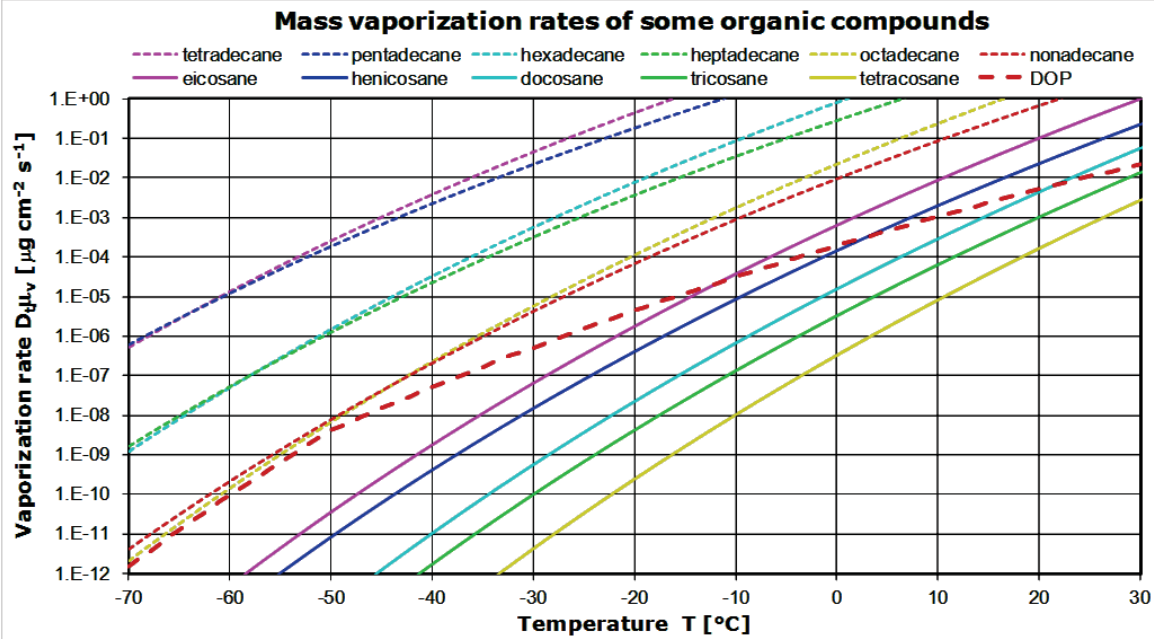

Figure 7. Temperature dependence of the mass vaporization rate of several simple organic compounds. Note the strong dependence upon temperature, which is related to the vaporization enthalpy of the compound[11].

In turning OFF the ACIS detector-housing heater, the *Chandra* team may have inadvertently performed an experiment on OBF contamination. If the more rapid accumulation starting about 2009 indeed resulted from slower vaporization of contamination due to lower temperatures, this "experiment" may indicate that at least some of the contamination has a volatility in a range that moderate elevation of the temperature could remove it. The fact that the mass column near the OBF centers is less than that near the OBF edges also suggests that some of the contamination is vaporizing at a rate comparable to the deposition rate. These considerations have engendered optimism that partial cleaning of the OBFs may be possible. For this reason, we have begun a new contamination-migration study (§3) employing a higher-fidelity model of the ACIS cavity

3. MODELING METHODOLOGY AND RESULTS

In order to simulate contamination migration aboard the observatory, we first construct a high-fidelity geometric model (§3.1)—comprised of a large number of surface elements—of the relevant optical cavity. Given the geometric model, we next use thermal properties and boundary conditions to generate a thermal model (§3.2) to determine the temperature of each surface element. Given the thermal model, we then use molecular-volatility properties, surface temperatures, and other boundary conditions—including external contamination sources and sinks (vents)—to model molecular transport (§3.3) within the optical cavity.

3.1. Geometric model

For our first *Chandra* contamination-migration study[10], we developed a moderate-fidelity geometric model of the entire optical cavity—Telescope cavity (basically, the contents of the optical bench, Figure 1) and ACIS cavity (Figure 2), plus a short connecting conduit. In performing the thermal and molecular-transport analyses, we realized that the Telescope-cavity geometry was much more detailed than necessary but that the ACIS-cavity geometry lacked sufficient detail and resolution to provide a high-fidelity simulation of contamination of the ACIS OBFs.

Figure 8 displays the geometric model employed in the current study. The external view (left panel) illustrates the simplified treatment of the Telescope cavity and of the conduit to the ACIS cavity, which we justifiably reduced to a Telescope Closeout and Translation-table Closeout, respectively. These two closeouts comprise a small number of relatively large surface elements, onto which we may apply relatively straightforward, coarse-scale boundary conditions. In contrast, the internal view (right panel) depicts the more complicated treatment of the ACIS cavity. The higher-fidelity ACIS-cavity geometry model not only provides much higher resolution for surfaces of interest (especially the OBFs) but also includes potentially important features (such as the frame surrounding and protruding slightly above the OBF surfaces). The new ACIS geometry model covers 0.66 m^2 comprising 919 nodes—0.50 m^2 comprising 738 nodes within the ACIS cavity—including 121 OBF-I and 203 OBF-S nodes.

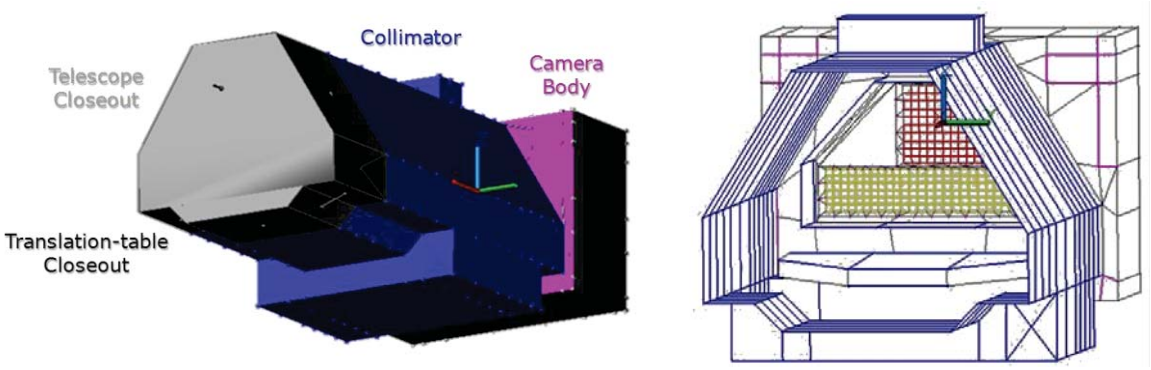

Figure 8. Geometric model for the *Chandra* optical cavity, used for the thermal analysis and for the molecular-transport analysis in the current study. The external view (left panel) illustrates the simplified treatment of the geometry outside the ACIS cavity; the interior view (right panel) displays the more complex treatment of the geometry within the ACIS cavity, especially for the optical blocking filters OBF-I (red square grid) and OBF-S (yellow rectangular grid).

For the current study, we utilized the software tool Thermal Desktop™ (C&R Technology), which has more capability for geometric modeling and analysis than did older tools (e.g., TRASYS) used previously. RADCAD, a sub-module of Thermal Desktop, calculates the geometric view factors (Figure 9), which govern the (radiative or molecular) transport from each surface element to the remaining surface elements. The vector A_j of surface areas and the matrix f_{jk} of view factors totally specify the geometric model for the transport simulations, used for the thermal model (§3.2) and for the molecular-transport model (§3.3).

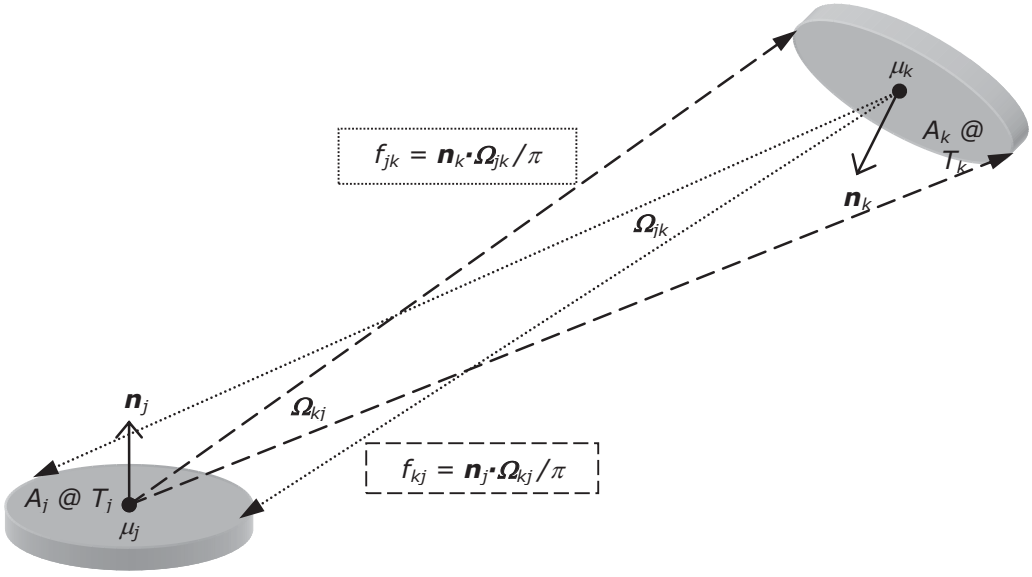

Figure 9. Drawing illustrating the definition of the geometric "view factor", used in analyses of (radiative or molecular) transport amongst surfaces. As the view factor specifies the fraction of the flux from one surface impingent upon a second surface, it is an essential geometric attribute in (radiative or molecular) transport analyses.

3.2. Thermal model

In addition to the geometry model, the thermal analysis requires specification of the radiative emissivity ε_j for each surface element, conductive linkages amongst elements, and the thermal boundary conditions. For this study, instead of performing a detailed thermal analysis of the entire spacecraft to predict ACIS temperatures, we employed flight telemetry data as boundary conditions for the thermal model. We binned thermal telemetry for 2008 through 2011 into 1-hour averages and then applied a conductive boundary to the ACIS collimator feet, camera body and focal plane. To solve the transient thermal model, we used the Thermal Desktop sub-module SINDA FLUINT to calculate the temperature T_j of each element.

In order to establish radiative boundary conditions at the Telescope Closeout (Figure 8 left panel), we modeled temperatures within the Telescope cavity. For the detailed thermal history at 1-hour resolution, we set the radiative sink at the Telescope Closeout to +12°C when ACIS was in the observing position or to a telemetered boundary temperature when ACIS was stowed. We ran the thermal model for the years 2008—during which the ACIS detector-housing heater was turned from ON to OFF—and 2011, obtaining temperature histories for ACIS-cavity surface elements.

Figure 10 compares the temperature distribution over the ACIS instrument with the detector-housing heater ON (left panel) in early 2008 to that with the detector-housing heater OFF (right panel) in late 2008. As the ACIS camera body, OBF frames, and snoot are aluminum and tightly linked conductively, these structures are nearly isothermal at the camera-body temperature recorded onboard (Figure 6), which is a boundary condition to the thermal model. Consequently, the temperature of the OBF frames is well-determined—namely, nearly equal to the recorded temperature of the ACIS camera body—essentially independent of the detailed thermal model developed here.

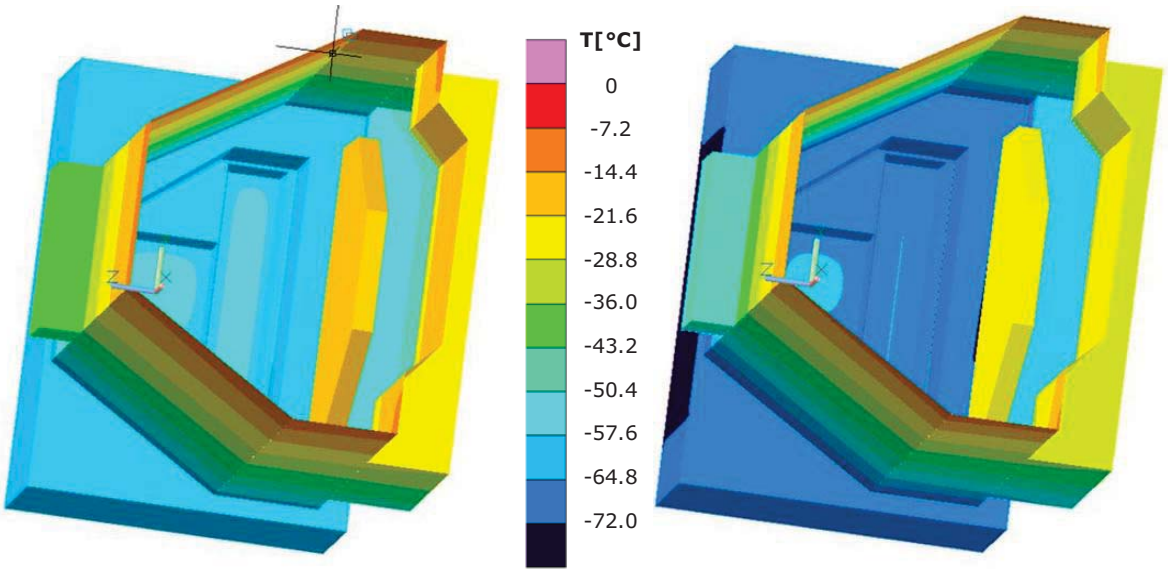

Figure 10. Temperature distribution over the ACIS instrument, for the detector-housing heater ON (left panel, early 2008) or for it OFF (right panel, late 2008). With the heater ON, the temperature of the camera body and OBF frames is about -61°C; with the heater OFF, about -69°C (Figure 6).

Unlike the conductively coupled surrounding surfaces, the OBF surfaces are mainly radiatively coupled. Figure 11 compares the temperature distribution over the OBFs with the detector-housing heater ON (left panel) in early 2008 to that with the detector-housing heater OFF (right panel) in late 2008. The thermal model displayed here sets the emissivity of the OBFs to $\varepsilon = 0.05$, the same as pristine aluminized polyimide. The emissivity of the contaminated OBFs is likely to be substantially higher and to increase with thickness of the contaminant (at least initially).

To estimate the importance of this effect, we performed a preliminary sensitivity study of the dependence of OBF temperature upon OBF emissivity for a case with the ACIS detector-housing heater OFF. The maximum OBF temperature is indeed sensitive to the assumed emissivity: -55.8°C, -46.5°C, -41.7°C, or -42.3°C for $\varepsilon_{OBF} = 0.05$, 0.10, 0.20, and 0.40, respectively. As discussed earlier (§2.2, Figure 7), temperature differences of this size significantly alter the mass vaporization rate of a molecular contaminant.

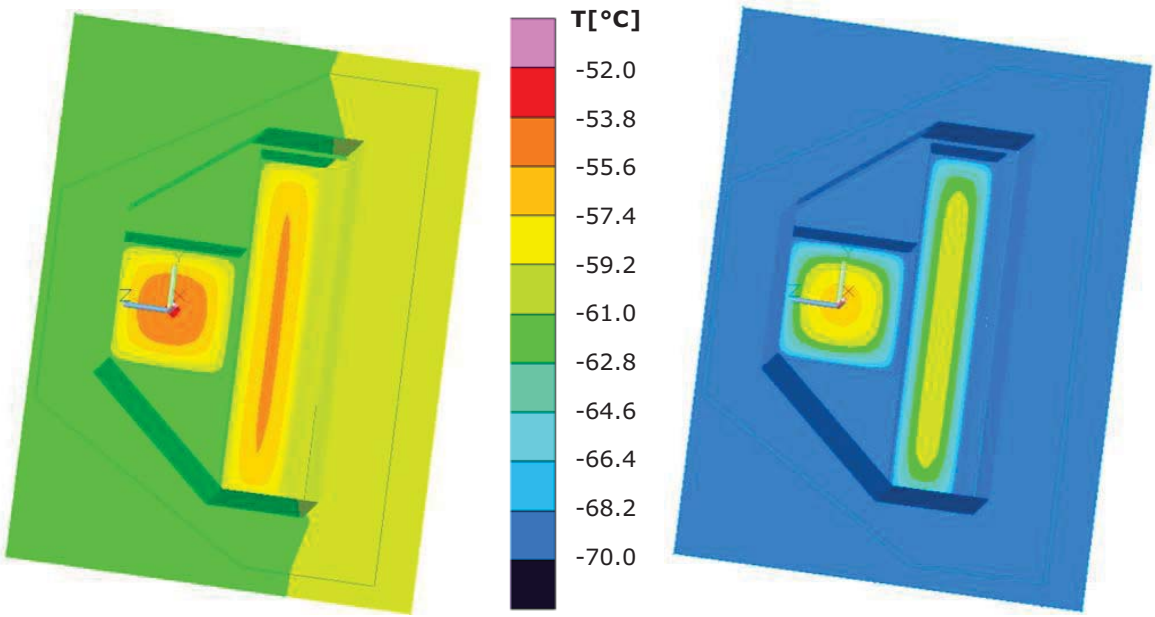

Figure 11. Temperature distribution over the ACIS camera top, including the optical blocking filters (OBF), for the detector-housing heater ON (left panel, early 2008) or for the heater OFF (right panel, late 2008). With the heater ON, the temperature near the center of OBF-I about -55°C; with the heater OFF, about -58°C. These thermal calculations assume that the emissivity of the OBFs is ε = 0.05, the same as pristine aluminum foil.

3.3. Molecular-transport model

The calculation of molecular transport is quite similar to the calculation of radiative transport in the thermal model (§3.2). Here we employ essentially the same methodology as we used in our previous study of contamination migration[10].

The molecular-transport model requires as input the area A_j, view factor f_{jk}, and temperature T_j for each surface element j: The geometry model (§3.1) calculates A_j and f_{jk}: the thermal model (§3.2), T_j. The transport equation calculates the evolution of the mass column μ_j of the contaminant on each surface element j, where the accumulation rate onto surface j is simply the deposition rate due to vaporization from all other surfaces k onto j (and to external sources), minus the vaporization rate from surface j:

$$\frac{d\mu_j}{dt} = +\left\{\sum_k \dot{\mu}_v(T_k)\Theta(\mu_k)\, f_{jk}\, \frac{A_k}{A_j}\right\} - \left\{\dot{\mu}_v(T_j)\Theta(\mu_j)\right\},$$

where $\dot{\mu}_v(T_j)$ is the mass vaporization rate as a function of the temperature T_j (e.g., Figure 7) on surface element j and the unit step distribution $\Theta(\mu_j)$ enforces the physical condition that the mass column must remain non-negative. As boundary conditions on the exchange of material between the ACIS cavity and the Telescope cavity, we treat the Telescope Closeout as a source and sink for material in the ACIS cavity.

The rate of vaporization—evaporation or sublimation, as appropriate to the phase of the deposited species—is simply related to the vapor pressure $P_v(T)$ through

$$\dot{\mu}_v(T) = \frac{P_v(T)}{\sqrt{2\pi\, RT/M}},$$

with R the ideal gas constant and M the molar mass of the contaminant. To determine the temperature dependence of the vapor pressure and mass vaporization rate, we apply the Clausius-Clapeyron relation to obtain $P_v(T)$ or $\dot{\mu}_v(T)$ at temperature T as a function of its value at a reference temperature T_o:

$$P_v(T) = P_v(T_\circ)\exp\left[-\frac{\Delta_v H}{R}\left(\frac{1}{T}-\frac{1}{T_\circ}\right)\right]$$

$$\dot{\mu}_v(T) = \dot{\mu}_v(T_\circ)\sqrt{\frac{T_\circ}{T}}\exp\left[-\frac{\Delta_v H}{R}\left(\frac{1}{T}-\frac{1}{T_\circ}\right)\right]$$

where the vaporization (evaporation or sublimation, as appropriate) enthalpy $\Delta_v H$ governs the temperature sensitivity. Figure 7 uses the above equations to plot the vaporization rate $\dot{\mu}_v(T)$ for several simple organic compounds, using tabulated values for $P_v(T_\circ)$ and $\Delta_v H$.

We have just begun running contamination-migration simulations using the new models described above. Figure 12 exhibits results of exploratory contamination-migration simulations, under identical thermal conditions, for a contaminant of relatively low volatility (left panel) and for one of relatively moderate volatility (right panel). For relatively low volatility (left panel), the accumulation is deposition-dominated and peaked near the OBF's center, due to shadowing effects in the deposition. For relatively moderate volatility (right panel), the evaporation rate on the warmer parts of the OBF is comparable to the deposition rate, resulting in less accumulation near the (warmer) center of the respective OBF than near its (cooler) edge. For relatively high volatility (not shown), evaporation dominates deposition and the OBF would clean, starting from the (warmer) center out to the (cooler) frame.

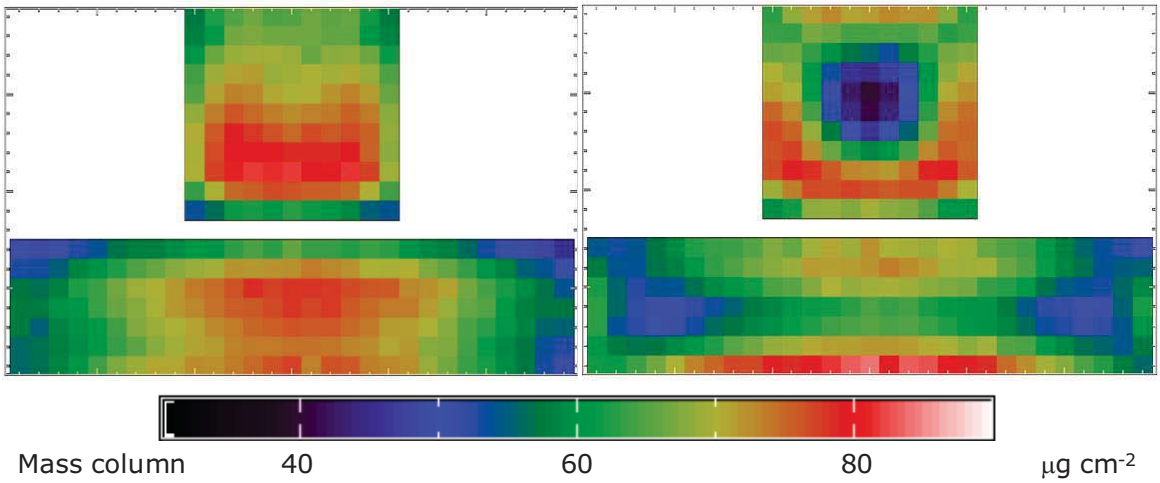

Figure 12. Distribution of mass column of accumulated molecular contamination on the ACIS OBFs, based upon molecular-transport simulations for a contaminant with relatively low volatility (left panel) and for one with a relatively moderate volatility (right panel). These molecular-transport calculations use OBF temperatures determined assuming that the emissivity of the OBFs is ε = 0.05, the same as pristine aluminum foil.

The fact that the observed distribution of contamination on the ACIS OBFs (§2.1, Figure 4) more closely resembles Figure 12 right panel than the left panel indicates that the volatility of the contaminant is such that evaporation is competitive with deposition over at least the warmer areas of the OBFs. This has engendered some optimism that it may be possible to develop a heating procedure to promote cleaning of the OBFs. Thus, we anticipate using contamination-migration simulations to assess various scenarios for cleaning the OBFs.

4. SUMMARY

Although we are optimistic about potentially cleaning the OBFs (at least partially), we recognize that there are significant uncertainties in the modeling. We are comfortable with the fidelity and accuracy of the geometric model (§3.1) and with most of the thermal model (§3.2), which is largely conductively coupled and utilizes actual onboard temperature measurements. Unfortunately, by far the greatest uncertainty in the thermal modeling is the temperature distribution on the contaminated OBFs. As the OBFs are predominantly radiatively coupled, their temperature distribution is sensitive to the emissivity ε of their surfaces (§3.2), which in turn depends upon the thickness and properties of the contaminant(s) on its surfaces.

For the exploratory simulations here (Figure 12), we used a thermal model with the emissivity of the ACIS OBFs set to $\varepsilon = 0.05$—i.e., the emissivity of the pristine filter. The emissivity of the contaminated OBF surface is likely to be significantly larger and non-uniform due to non-uniformity of the accumulated contamination across the OBF. Uncertainty in the distribution of ε across the OBFs produces uncertainty in the temperature distribution, which results in uncertainty in the vaporization rate and, thus, in the accumulation rate of the contaminant(s). Consequently, physically accurate modeling of the accumulation of contaminant(s) on the OBF surface will require more complicated, iterative thermal and molecular-transport simulations.

It is interesting to note that the coupling between emissivity, temperature, and contaminant mass column (or thickness) is possibly quasi-self-regulating for contaminant(s) with relatively moderate volatilities—i.e. comparable vaporization and deposition rates. As the contaminant accumulates, the emissivity increases, thus raising the temperature and the vaporization rate, which in turn reduces the accumulation rate.

The other major uncertainty in the modeling is that we have not identified the species of the molecular contaminant(s). With prior knowledge of neither the deposition rate nor the vaporization properties of the contaminant(s), we shall need to explore a large volume of parameter space. Hopefully, comparing simulation results with the observed evolution of the mass column will sufficiently constrain the properties of the contaminant(s) to provide confidence simulations of possible cleaning scenarios.

ACKNOWLEDGEMENTS

The *Chandra X-ray Observatory* is operated by the Smithsonian Astrophysical Observatory (SAO) under contract to NASA Marshall Space Flight Center (MSFC). The Advanced CCD Imaging Spectrometer (ACIS) was developed by the Massachusetts Institute of Technology (MIT) and Pennsylvania State University.

REFERENCES

[1] Weisskopf, M. C., "The Chandra X-Ray Observatory: progress report and highlights", Proc. SPIE 8443, 0Y 9pp (2012).

[2] Weisskopf, M. C, Aldcroft, T. L., Bautz, M., Cameron, R. A., Dewey, D., Drake, J. J., Grant, C. E., Marshall, H. L., & Murray, S. S., "An overview of the performance of the Chandra X-ray Observatory", Exp. Astron. 16, 1–68 (2003).

[3] Weisskopf, M. C., Brinkman, B., Canizares, C., Garmire, G., Murray, S., & Van Speybroeck, L. P., "An overview of the performance and scientific results from the Chandra X-ray Observatory", Pub. Astron. Soc. Pacific 114, 1–24 (2002).

[4] Weisskopf, M. C., Tananbaum, H. D., Van Speybroeck, L. P., & O'Dell, S. L., "Chandra X-ray Observatory (CXO): overview", Proc. SPIE 4012, 2–16 (2000).

[5] Garmire, G. P., Bautz, M. W., Ford, P. G., Nousek, J. A., & Ricker, G. R., Jr., "Advanced CCD Imaging Spectrometer (ACIS) instrument on the Chandra X-ray Observatory", Proc. SPIE 4851, 28–44 (2003).

[6] Powell, F. R., Keski-Kuha, R. A., Zombeck, M. V., Goddard, R. E., Chartas, G., Townsley, L. K., Moebius, E., Davis, J. M., & Mason, G. M., "Metalized polyimide filters for x-ray astronomy and other applications", SPIE 3113, 432–440 (1997).

[7] Plucinsky, P. P., Schulz, N. S., Marshall, H. L., Grant, C. E., Chartas, G., Sanwal, D., Teter, M., Vikhlinin, A. A., Edgar, R. J., Wise, M. W., Allen, G. E., Virani, S. N., DePasquale, J. M., & Raley, M. T., "Flight spectral response of the ACIS instrument", Proc. SPIE 4851, 89−100 (2003).

[8] Plucinsky, P. P., O'Dell, S. L., Tice, N. W., Swartz, D. A., Bautz, M. W., DePasquale, J. M., Edgar, R. J., Garmire, G. P., Giordano, R., Grant, C. E., Knollenberg, P., Kissel, S., LaMarr, B., Logan, R., Mach, M., Marshall, H. L., McKendrick, L., Prigozhin, G. Y., Schwartz, D., Schulz, N. S., Shropshire, D., Trinh, T., Vikhlinin, A. A., & Virani, S. N., "An evaluation of a bake-out of the ACIS instrument on the Chandra X-Ray Observatory", Proc. SPIE 5488, 251−263 (2004).

[9] Marshall, H. L., Tennant, A., Grant, C. E., Hitchcock, A. P., O'Dell, S. L., & Plucinsky, P. P., "Composition of the Chandra ACIS contaminant", Proc. SPIE 5165, 497−508 (2004).

[10] O'Dell, S. L., Swartz, D. A., Plucinsky, P. P., Freeman, M. A., Markevitch, M. L., Vikhlinin, A. A., Chen, K. C., Giordano, R. J., Knollenberg, P. J., Morris, P. A., Tran, H., Tice, N. W., & Anderson, S. K., "Modeling contamination migration on the Chandra X-ray Observatory", Proc. SPIE 5898, 313−324 (2005).

[11] Acree, W., & Chickos, J. S., "Phase transition enthalpy measurements of organic and organometallic compounds. Sublimation, vaporization, and fusion enthalpies from 1880 to 2010", J. Phys. Chem. Ref. Data 39, 043101 942pp (2010).